Received: 23 July 2024 | Revised: 16 October 2024 | Accepted: 17 October 2024

DOI: 10.1002/nbm.5289

RESEARCH ARTICLE

NMR IN BIOMEDICINE WILEY

A signal model for fat-suppressed T_1-mapping and dynamic contrast-enhanced MRI with interrupted spoiled gradient-echo readout

Myrte Wennen[1,2] | Wilhelm Stehling[1] | J. Tim Marcus[1] | Joost P. A. Kuijer[1] | Cristina Lavini[1] | Leo M. A. Heunks[3] | Gustav J. Strijkers[4] | Bram F. Coolen[4] | Aart J. Nederveen[1] | Oliver J. Gurney-Champion[1,5]

[1]Department of Radiology and Nuclear Medicine, Amsterdam University Medical Center, Amsterdam, The Netherlands

[2]Department of Intensive Care, Erasmus Medical Center, Rotterdam, The Netherlands

[3]Department of Intensive Care, Radboud University Medical Center, Nijmegen, The Netherlands

[4]Department of Biomedical Engineering & Physics, Amsterdam University Medical Center, Amsterdam, The Netherlands

[5]Cancer Center Amsterdam, Imaging and Biomarkers, Amsterdam, The Netherlands

Correspondence
M. Wennen, Department of Radiology and Nuclear Medicine, Amsterdam University Medical Center, Amsterdam, The Netherlands.
Email: m.wennen@amsterdamumc.nl

Funding information
ZonMw, Grant/Award Number: 09120011910004; KWF-UVA, Grant/Award Number: 2021.13785

Abstract

The conventional gradient-echo steady-state signal model is the basis of various spoiled gradient-echo (SPGR) based quantitative MRI models, including variable flip angle (VFA) MRI and dynamic contrast-enhanced MRI (DCE). However, including preparation pulses, such as fat suppression or saturation bands, disrupts the steady-state and leads to a bias in T_1 and DCE parameter estimates. This work introduces a signal model that improves the accuracy of VFA T_1-mapping and DCE for interrupted spoiled gradient-echo (I-SPGR) acquisitions. The proposed model was applied to a VFA T_1-mapping I-SPGR sequence in the Gold Standard T_1-phantom (3 T), in the brain of four healthy volunteers (3 T), and to an abdominal DCE examination (1.5 T). T_1-values obtained with the proposed and conventional model were compared to reference T_1-values. Bland–Altman analysis (phantom) and analysis of variance (in vivo) were used to test whether bias from both methods was significantly different ($p = 0.05$). The proposed model outperformed the conventional model by decreasing the bias in the phantom with respect to the phantom reference values (mean bias -2 vs. -35% at 3 T) and in vivo with respect to the conventional SPGR (-6 vs. -37% bias in T_1, $p < 0.01$). The proposed signal model estimated approximately 48% (depending on baseline T_1) higher contrast concentrations in vivo, which resulted in decreased DCE pharmacokinetic parameter estimates of up to 35%. The proposed signal model improves the accuracy of quantitative parameter estimation from disrupted steady-state I-SPGR sequences. It therefore provides a flexible method for applying fat suppression, saturation bands, and other preparation pulses in VFA T_1-mapping and DCE.

KEYWORDS
dynamic contrast-enhanced MRI, fat suppression, spoiled gradient echo, T_1-mapping, variable flip angle

Abbreviations: AIF, arterial input function; DCE MRI, dynamic contrast-enhanced magnetic resonance imaging; FFE, fast field echo; FLASH, fast low-angle shot; GRASP, golden-angle radial sparse parallel; I-SPGR, interrupted spoiled gradient-echo; LPS, lines per shot; OSIPI, open science initiative for perfusion imaging; QIBA, quantitative imaging and biomarkers alliance; SPGR, spoiled gradient-echo; TFE, turbo field echo; VFA, variable flip angle.

1 | INTRODUCTION

Quantitative measurement of tissue microstructure using T_1-mapping and dynamic contrast-enhanced (DCE) MRI has the potential for diagnosis, response prediction, and response monitoring in multiple medical fields, including oncology, cardiology, and musculoskeletal applications.[1–5] During T_1-mapping, T_1 is quantified based on multiple MRI acquisitions with different T_1 weightings. This is achieved, for example, by varying flip angles (VFA), inversion times, or repetition times. Furthermore, T_1-mapping, typically VFA, forms the basis of DCE MRI. In DCE MRI, the characteristics of the tissue microenvironment, such as permeability, and vascular and extravascular volumes, are estimated based on T_1 changes after injection of a bolus of a gadolinium-based contrast agent.[6,7] The contrast agent affects local T_1, and changes in T_1 are directly related to the local contrast agent concentration. Hence, DCE is typically acquired using T_1-weighted sequences,- and knowing the correct relation between the signal and T_1 is the basis for DCE analysis.

In T_1-mapping and DCE MRI, images are typically measured with a spoiled gradient echo (SPGR) sequence with steady-state magnetization, referred to as 'fast field echo' (FFE), 'fast low-angle shot' (FLASH), and 'SPGR' depending on the vendor. This steady-state sequence allows for a relatively straightforward signal modeling. However, to improve image quality, SPGR acquisitions can be performed with preparation pulses interrupting the acquisition shots (Figure 1, I-SPGR), for example, fat suppression pulses and saturation bands.[8–10] These sequences are termed by vendors as 'Turbo field echo' (TFE), 'Turbo FLASH', and 'fast SPGR'. Fat suppression in VFA T_1-mapping and DCE MRI is especially beneficial as the bright signal from fat can obscure the region of interest and fat suppression prevents artifacts due to water-fat shift.[11] Radial acquisitions, such as the golden-angle radial sparse parallel (GRASP) acquisition, benefit from fat suppression because they are highly susceptible to off-resonance effects.[12] Particularly in abdominal imaging, where fat suppression is crucial, the inclusion of preparation pulses is therefore highly desirable. The I-SPGR sequences can also include inversion or saturation pulses to, for example, enhance T_1-weighting. In this work, we only refer to the use of these sequences without inversion or saturation pulses because they violate the signal model generally used for VFA T_1-mapping and DCE MRI.

An important drawback of using I-SPGR sequences in quantitative imaging is that the use of preparation pulses disrupts the steady-state magnetization, which can thereby introduce a systematic bias in T_1-mapping and DCE parameter estimates.[13,14] Previous research by Ikeno et al. has indeed shown that the precision and accuracy of T_1-mapping decreases when using fat suppression techniques.[14] As the DCE MRI signal is based on the T_1-altering effects of the contrast agent, the decreased accuracy also results in incorrect calculation of contrast concentrations and, consequently, pharmacokinetic parameters. Therefore, the Quantitative Imaging Biomarkers Alliance (QIBA) guidelines advise against the use of fat suppression.[15] Despite this advice, numerous studies did use I-SPGR for both VFA T_1–mapping and DCE MRI, without accounting for the disruption of steady-state [e.g.,10,16–18] further highlighting the role of fat-suppression in such sequences. The results of those studies, however, may be biased as a consequence.

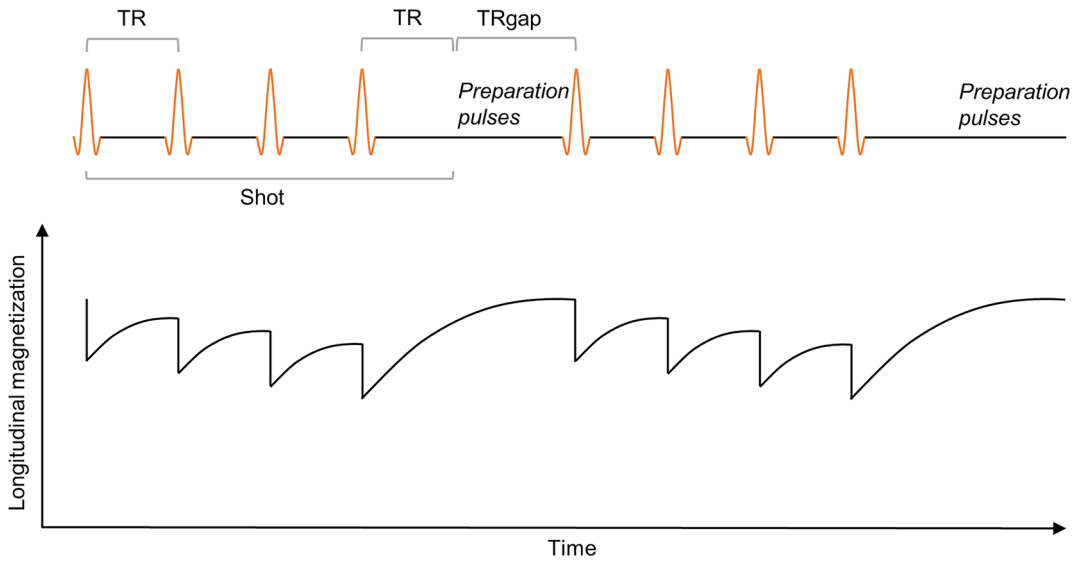

FIGURE 1 Pulse sequence diagram for the RF pulses (top) and a sketch of the corresponding longitudinal magnetization (bottom) for an interrupted gradientecho sequence. The RF pulses in one shot are followed by a temporal gap that can contain fat suppression and/or other preparation steps such as saturation bands. The contrast is predominantly defined at the center of the k-space, which is acquired after *n* RF pulses within the shot, depending on the k-space filling strategy used.

In this study, we therefore aimed to find a simple strategy to compensate for the interruption in steady-state caused by preparation pulses that do not affect the spins in the region of interest. We introduce an adapted signal model and compare its accuracy to the accuracy of the conventional steady-state model. To show the feasibility and validity of our approach, the model was tested in a T_1-phantom using MR scanners from two different vendors and in vivo in the brains of healthy volunteers. Furthermore, the effect of the adjusted signal model on the pharmacokinetic parameters of the abdominal organs was tested in a DCE MRI acquisition in a healthy volunteer.

2 | THEORY

In a regular steady-state spoiled gradient-echo sequence, the signal equation is given by:

$$S = M_0 \sin(\alpha) \frac{1 - \exp(-TR/T_1)}{1 - \exp(-TR/T_1)\cos(\alpha)}, \tag{1}$$

where S is the acquired signal; M_0 is the proton density; T_1 is the longitudinal relaxation time; TR is the repetition time of the sequence; and α is the flip angle of the RF pulses. Using Equation (1), T_1 and M_0 are typically estimated from a series of images acquired at different flip angles by, for example, least squares fitting of the signal. In practice, that means that M_0 also serves as a scaling factor. In an I-SPGR sequence, the normal steady-state in the SPGR is interrupted by a temporal gap every k RF excitation pulses (Figure 1, TR_{gap}). TR_{gap} starts one TR after the last RF pulse of the shot and ends at the first RF pulse of the next shot. This gap can be used for fat suppression, a spatial pre-saturation pulse, and/or potential other preparing pulses. The parameter k is defined as the number of RF pulses per shot (also called lines per shot or turbo factor) and includes potential start-up echoes. We define a "shot" as the set of RF pulses, including the temporal gap, that is being repeated (Figure 1).

To correct for the interruption of the steady-state, we derived a signal equation. If the preparation modules are not affecting the magnetization of the water spins of interest (for example spectral fat suppression pulses or saturation slabs) then, for each shot, the longitudinal magnetization at the end of the gap (M_{endGap}) is equal to the magnetization at the start ($M_{startGap}M_{startGap}$) with additional T_1-relaxation that occurred during the gap:

$$M_{endGap} = M_{startGap} + (M_0 - M_{startGap})(1 - E_{1,gap}) = M_{startGap}E_{1,gap} + M_0(1 - E_{1,gap}), \tag{2}$$

with $E_{1,gap} = \exp(-TR_{gap}/T_1)$.

In general, when an RF pulse is given, after one repetition time, the proposed magnetization along the longitudinal axis (M_{l+1}) can be written as a recursive formula as a function of the magnetization after the previous RF pulse (M_l) as:

$$M_{l+1} = M_l \cos(\alpha) + (M_0 - M_l \cos(\alpha))(1 - E_1), \tag{3}$$

with $E_1 = \exp(-TR/T_1)$, where the first term before the plus sign takes into account the loss in longitudinal magnetization due to the RF pulse and the second term takes into account the gain in longitudinal magnetization due to T_1 relaxation. Taking M_{endGap} as an initial point, this recursive formula allows calculating the longitudinal magnetization after n RF pulses and TRs as:

$$M_n = M_{endGap}(E_1\cos(\alpha))^n + M_0(1 - E_1)\frac{1 - (E_1\cos(\alpha))^n}{1 - E_1\cos(\alpha)}. \tag{4}$$

If we define k as the number of RF pulses between two gaps, then $M_{startGap}$ can be found by replacing n for k and noting that $M_{startGap}$ equals M_k. Because of the steady-state over every shot, $M_{startGap}$ is equal to the $M_{startGap}$ from the previous shot. Adding [2] into [4] and replacing n by k then gives:

$$M_{startGap} = M_k = (M_{startGap}E_{1,gap} + M_0(1 - E_{1,gap}))(E_1\cos(\alpha))^k + M_0(1 - E_1)\frac{1 - (E_1\cos(\alpha))^k}{1 - E1\cos(\alpha)}. \tag{5}$$

Solving for $M_{startGap}$ and combining with Equation (2) results in:

$$M_{endGap} = M_0 \left[\left[\frac{(1-E_{1,gap})(E_1\cos(\alpha))^k + (1-E_1)\frac{1-(E_1\cos(\alpha))^k}{1-E_1\cos(\alpha)}}{\left(1-E_{1,gap}(E_1\cos(\alpha))^k\right)} \right] E_{1,gap} + (1-E_{1,gap}) \right]. \quad (6)$$

The signal (transverse magnetization, S) directly after the gap equals $S = M_{endGap}\sin(\alpha)$ and thus n TR's after the gap, this signal is:

$$S_n = M_{n-1}\sin(\alpha), \quad (7)$$

where M_{n-1} is the longitudinal magnetization n-1 pulses after the gap. Including the effect of $n-1$ RF pulses in Equation (4) and combining it with Equation (6) can be used to express M_{n-1}. Adding M_{n-1} in Equation (7) gives the final signal equation:

$$S(\alpha, TR, TRgap, k, n) = \left[\left[\left[\frac{(1-E_{1,gap})(E_1\cos(\alpha))^k + (1-E_1)\frac{1-(E_1\cos(\alpha))^k}{1-E_1\cos(\alpha)}}{\left(1-E_{1,gap}(E_1\cos(\alpha))^k\right)} \right] E_{1,gap} + (1-E_{1,gap}) \right] (E_1\cos(\alpha))^{n-1} + (1-E_1)\frac{1-(E_1\cos(\alpha))^{n-1}}{1-E_1\cos(\alpha)} \right] \sin(\alpha) M_0. \quad (8)$$

This equation allows us to estimate T_1 from S by repeating an I-SPGR acquisition while varying one of the acquisition parameters α, TR, TR_{gap}, k, and n. In this work, we only focus on varying the flip angle α (VFA T_1-mapping). Building upon the assumption that the overall signal contrast of MRI images is predominantly defined by the signal in the center of k-space, we can use Equation (8) to describe the signal in the image when n is the number of RF pulses before we reach the center of k-space. For example, $n = 1$ for a centric (also known as low-high) k-space filling and no startup echoes.

As multiple applications make use of SPGR read-outs that adhere to the same physical principles, versions of the derived signal model have been used in other work before, but only with the inclusion of inversion pulses. Brix et al (1990) derived a similar equation and used this equation for inversion-recovery T_1-mapping.[19] Additionally, the signal model behind the MP2RAGE sequence also overlaps with the model in Equation (8).[20,21]

2.1 | DCE MRI

DCE MRI requires the computation of the concentration of the contrast agent over time ($C[t]$), based on the change in T_1 after contrast injection. For conventional SPGR, the change in T_1 is determined based on the inversion of Equation (1), resulting in:

$$T_1(t) = \frac{-TR}{\ln\left(A - \frac{S(t)}{S_0}\right) - \ln\left(A - \frac{S(t)}{S_0}\cos(\alpha)\right)}, \quad (9)$$

with $A = \frac{1-\cos(\alpha)\exp(-TR/T_1)}{1-\exp(-TR/T_1)}$ and S_0 the signal before contrast injection. After computing T_1 over time, the contrast concentration over time in the tissue ($C[t]$) is determined from the T_1 values, the baseline T_1 (T_{10}), and the relaxivity of the contrast agent (r):

$$C(t) = \left(\frac{1}{T_1(t)} - \frac{1}{T_{10}}\right)\frac{1}{r}. \quad (10)$$

Subsequently, a pharmacokinetic model can be used to calculate tissue physiological parameters from the signal curve. Such models typically require an arterial input function, which represents the concentration of contrast agents in the arterial blood supply over time. For example, the extended Tofts model,

$$C(t) = v_p C_p(t) + K^{trans}\int_0^t C_p(\tau)e^{-\left(\frac{K^{trans}}{v_e}\right)(t-\tau)}d\tau, \quad (11)$$

mathematically describes the exchange of contrast between the vessel and surrounding extracellular, extravascular space, which allows estimating the transfer constant (K^{trans}), rate constant (k_{ep}), extracellular extravascular space (v_e), and blood plasma volume (v_p).[22] The extended Tofts model requires knowledge of the concentration in the plasma ($C_p[t]$), which can be determined on an individual or population basis, and this concentration curve is referred to as the arterial input function (AIF).

As Equation (8) cannot be inverted, for DCE, it is necessary to use voxel-wise fitting to estimate T_1 using M_0 as input, where M_0 is taken from the initial T_{10} fit. This results in a linear fit of Equation (8) for each time point, with one data point ($S[t]$) and one unknown parameter ($T_1[t]$). From that T_1 estimation, the contrast concentration can be obtained using Equation (10).

3 | METHODS

3.1 | Simulations

To gain insight in the extend of the expected bias, we simulated the bias introduced when the effect of the interruption of the steady--state is ignored. Because the bias will depend on sequence design, the I-SPGR VFA signal was simulated for different ranges of k, n, and TR_{gap} using the proposed signal model (Equation (8)). Then, T_1 was estimated by fitting this I-SPGR signal with the conventional equation (Equation (1)) to compute the bias. Other simulated parameters were kept the same as in the MR acquisition described below (Table 1, 3 T settings). The difference between the T_1 used to simulate the signal and the estimated T_1 was used to compute the bias.

It is known that the SPGR model is affected by noise and $B1^+$-field heterogeneity. Therefore, we additionally aimed to verify that the I-SPGR acquisition and model are impacted by noise and inhomogeneity of the $B1^+$-field to a similar extent as the SPGR model. These experiments are described in the Supplemental Material.

Lastly, we estimated the bias in contrast concentration measured in DCE by using the conventional signal model for I-SPGR DCE. We simulated a DCE experiment based on the in vivo DCE I-SPGR acquisition (Table 1). The DCE and VFA signals were simulated using Equation (8) with $T_{10} = 700$ ms, $M_0 = 10$, and by decreasing T_1 in steps of 5 ms to 100 ms as a simulation of contrast inflow that shortens T_1. Then, Equation (1) was used to fit T_{10} and with Equation (9) the T_1 for other 'time' steps was computed. With Equation (10), the concentration was computed with the simulated and computed T_1 for every step, assuming a longitudinal relaxivity of 3.80 1/s/mM.[23] These simulations also allow for validation of the results in vivo.

As fit algorithms are prone to end up in local minima, there are many advanced fitting routines used in VFA and DCE. Because we are interested in how well the models describe the data, we chose to use the least squares fit initiated with the ground truth parameters as starting values. Then, any deviation from the ground truth is not caused by a local minimum and must be inherent to the model that is fitted to the data.

TABLE 1 Sequence parameters for acquisitions in the phantom (3 T), healthy volunteers (3 T), and a DCE acquisition in a healthy volunteer (1.5 T).

	3 T (Philips)		1.5 T (Siemens)
Sequence title	**SPGR VFA (FFE)**	**I-SPGR VFA (TFE)**	**VFA- and DCE-GRASP**
Sequence type	Spoiled gradient-echo	Interrupted spoiled gradient-echo	Interrupted spoiled gradient-echo, interrupted, golden-angle radial stack-of-stars k-space filling
Repetition time (ms)	6.6	6.6	4.3
Echo time (ms)	3.2	3.2	1.3
Flip angle (°)	2, 5, 10, 15, 20, 25	2, 5, 10, 15, 20, 25 (high flip angle case: 30, 35, 40, 45, 50, 55)	5, 10, 12 (DCE), 15, 20
Field of view (mm)	220 x 220 x 45 (in vivo) 150 x 150 x 30 (phantom)	220 x 220 x 45 (in vivo) 150 x 150 x 30 (phantom)	380 x 380 x 216
Acquisition matrix (freq x phase x slices)	160 x 160 x 15 (in vivo) 188 x 188 x 15 (phantom)	160 x 160 x 15 (in vivo) 188 x 188 x 15 (phantom)	28 partitions, 512 readouts per spoke, 1990 spokes per partition
RF pulses per shot (k)	NA	25	28
Temporal gap (ms)	NA	35	37
Centre k-line (n)	NA	1 (centric), 13 (linear)	9 (linear)
RF spoiling phase angle (°)	117	117	50
Compressed sensing	No	No	Yes
Acquisition time	~ 2:45 min	~ 2:50 min	~3 min (VFA) ~5 min (DCE)
Additional information			Free-breathing, partial Fourier 5/8, spectral fat suppression pulses

3.2 | Data acquisition

We obtained phantom and in vivo VFA T_1-mapping data on a 3 T scanner (Ingenia Elition X, Philips, Best, The Netherlands). Eight T_1-vials (T_1 varying from 236 to 2013 ms and T_2 from 15 to 328 ms) of the MultiSample 120E (Gold Standard Phantoms, Sheffield, United Kingdom) phantom were imaged using VFA sequences with an SPGR and I-SPGR acquisition to validate T_1-mapping using a 16-channel head coil. A picture of the phantom can be found in the Supplemental Material (Figure S3). Secondly, the brains of four healthy subjects (two female, mean age 28 years) were imaged on the same scanner with both a I-SPGR and conventional SPGR sequence to verify the method in vivo.

Lastly, a T_1-weighted DCE acquisition of the abdomen was performed in a healthy volunteer using the compressed sensing GRASP Siemens product sequence on a 1.5 T scanner (Siemens MAGNETOM SOLA, Erlangen, Germany) during the injection of 0.1 mmol/kg DOTAREM® at 2 ml/s. GRASP is a I-SPGR sequence with fat suppression and two saturation bands. All subjects gave written informed consent, and the study was approved by the local ethics board.

3.3 | Sequence parameters

3D SPGR acquisitions at flip angles 2, 5, 10, 15, 20, and 25° were used for VFA T_1-mapping in the phantom and in vivo. The SPGR sequences were repeated with an I-SPGR sequence, in the form of a Cartesian-filled TFE (Philips) or a GRASP acquisition at 1.5 T (Siemens). As the I-SPGR signal shows phenomena at flip angles > 30° - the signal stabilizes or even increases as a function of flip angle - that cannot be explained by the SPGR signal model, the I-SPGR acquisition was also repeated at high flip angles (30, 35, 40, 50, and 55°). These measurements are only used to further validate the I-SPGR equation and to show the distinct difference between the conventional and proposed signal model (Figure 2). Further sequence details are listed in Table 1 (3 T) and Table S1 (1.5 T).

3.4 | Image processing

Voxel-wise fitting of T_1 and M_0 was performed using in-house written software in Matlab (R2022b, Natick, Massachusetts: The MathWorks Inc.). The initial guess was a T_1 of 1000 ms and M_0 as a signal in that voxel at the lowest acquired flip angle divided by the sine of that flip angle. The fit boundaries were 10–3000 ms for T_1 and $0–10^{10}$ for M_0. Fitting was performed based on Equation (1) (hereafter defined as the conventional

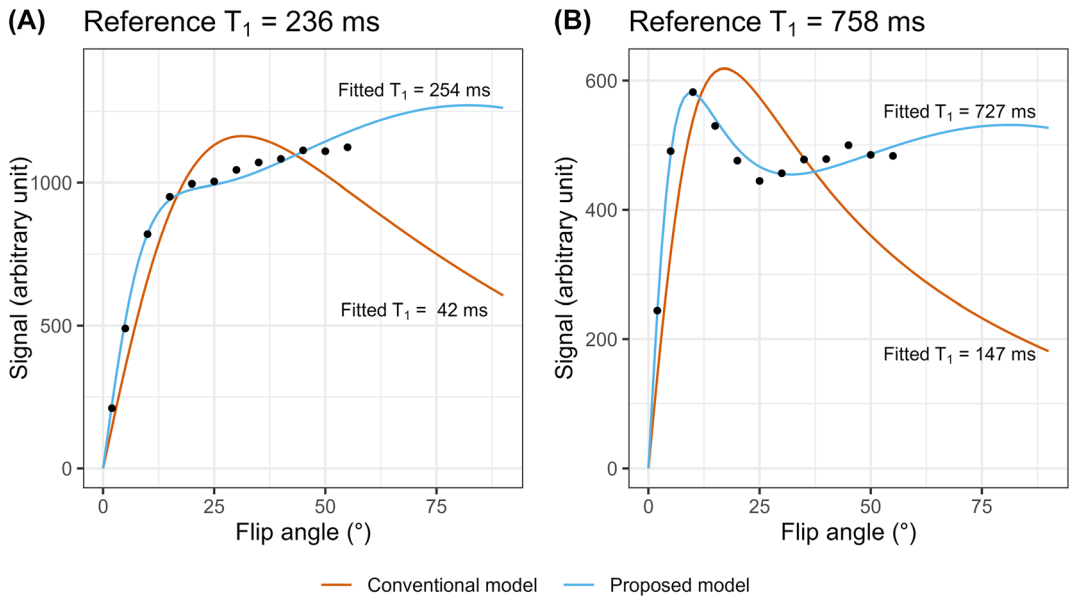

FIGURE 2 Example of curves fitted to the mean signal intensity of a region of interest within two spheres of the phantom with reference values $T_1 = 236$ ms (A) and $T_1 = 758$ ms (B). The two curves represent the fits with the conventional signal model (Equation (1), red line) and the proposed signal model (Equation (8), blue line). It can be appreciated that the fits performed with the conventional signal equation do not follow the data and return substantially underestimated T_1 values, while the proposed signal equation curve closely follows the data and gives more accurate T_1 estimates. The experiments at high flip angles were added to highlight the difference in signal evolution between the two models and are not used in the rest of the experiments.

approach) and [8] (hereafter defined as the proposed approach) using the Levenberg–Marquardt algorithm.[24] A Matlab script for simulating and fitting data is included as Supplemental Material. The script allows users to simulate the signal, add noise to the signal, and/or fit the conventional and proposed model. The script that fits the model can also be used for data acquired in a phantom or in vivo.

For the phantom, circular regions of interest (ROI) with fixed diameters were manually placed in the spheres in the fitted T_1 map. The mean and standard deviation of T_1 in these ROIs are reported and compared to the reference values mentioned in the phantom manual. In the in vivo brain data, a mask of the white and gray matter in one slice was created using the FMRIB Software Library (FSL, Oxford, UK). The mean and standard deviation of the T_1 values in the masks were computed and compared to the values measured with a conventional, non-interrupted SPGR VFA sequence within the same subject.

3.5 | DCE modeling

An abdominal DCE scan was obtained in a healthy volunteer. We measured a baseline T_1 map with a GRASP VFA sequence. The dynamic images were also obtained with GRASP and reconstructed offline using soft-weighting based on the respiratory signal obtained from the raw k-space data, using code available online.[25] From the dynamic DCE-GRASP images, the contrast concentration over time was calculated using the conventional approach (Equations (1), (9) and (10)) and using the adapted signal equation (Equations (8) and (10)). The relaxivity of the contrast agent required for Equation (10) was assumed to be 3.80 1/s/mM at 1.5 T.[23] DCE modeling was performed with code from the open science initiative for perfusion imaging (OSIPI).[26] For both cases, DCE modeling was done with an analytical version of the extended Tofts model (Equation (11)) (OSIPI: fit_tofts_model from src/original/OG_MO_AUMC_ICR_RMH_NL_UK/ExtendedTofts/DCE.py).[27] This model requires an analytical AIF, which was obtained by fitting to the signal in a region of interest in the aorta (individual AIF). To account for the additional perfusion via the portal vein in the liver, a separate dual inlet equation was used to compute the input functions and extended Tofts model parameters (Equation (11)) in the liver (OSIPI: DualInletExtendedTofts from/src/original/ST_USyd_AUS/ModelDictionary.py).[28]

For all models, we included both an individual and a population AIF to assess the effect of using the proposed model for both cases, as both types of AIFs are used in literature. The aortic AIF was taken from Klaassen et al (2020).[2] There is no population-based input function available for the portal vein input function required for the dual inlet model. Therefore the portal vein input function was always computed image-based and not population-based, where the portal vein input function computed with the conventional model was used as a surrogate for the population-based input function. In this way, the same portal vein input function was used for both the proposed and conventional models when the population-based AIF was used.

3.6 | Error measure and statistics

To quantify the bias of T_1-mapping, the mean T_1 values from the ROIs in the phantom and in vivo were compared to the reference values using the percentage difference:

$$Bias = \frac{T1_{measured} - T1_{reference}}{T1_{reference}} * 100\% \quad (12)$$

In the phantom, the reference values from the phantom manual were used. In the brain, a conventional SPGR VFA T_1 map served as a reference, because the use of the proposed model in an I-SPGR acquisition should result in the same measured T_1 as with the conventional SPGR approach.

Bland–Altman analysis was performed on the percentage difference between the ground truth and estimates (phantom) and the difference in T_1 between the SPGR and different fit approaches for I-SPGR (in vivo). Furthermore, the absolute difference in T_1 in vivo between the conventional and proposed signal model was tested for significance using an analysis of variance, including different subjects as a factor. $P < 0.05$ was considered significant.

4 | RESULTS

4.1 | Simulations

Simply ignoring the interruption of the steady state in I-SPGR acquisitions introduced a bias in the estimated T_1. Simulations showed that for the acquisition settings mentioned in Table 1 (I-SPGR VFA (TFE) – Philips 3 T, centric case), the bias was between 35 and 42%, depending on T_1

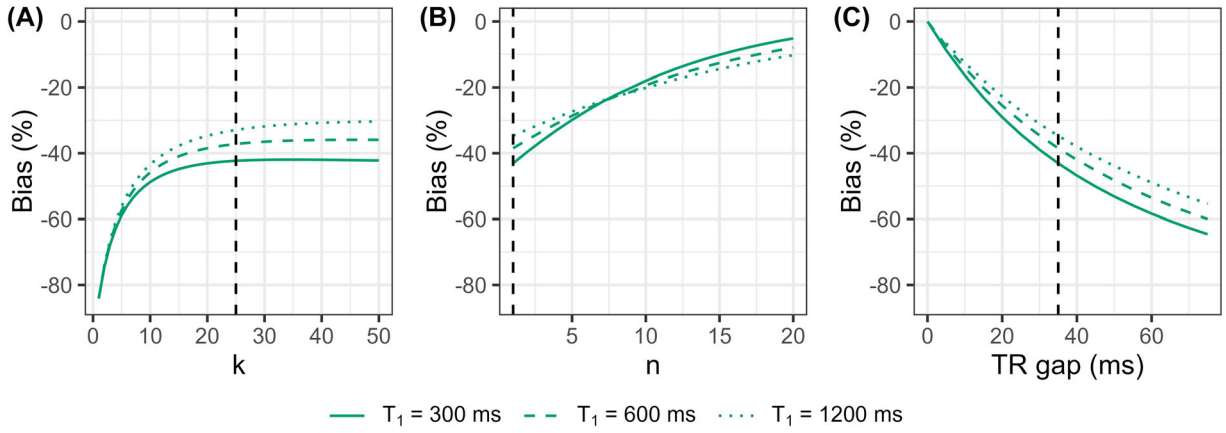

FIGURE 3 Effect of change in parameters k (number of RF pulses within one shot, A), n (at which RF pulses center of k-space is filled, B) and TR gap (duration of the temporal gap, C) on the bias resulting from using the conventional model (Equation (1)) in a I-SPGR acquisition, for different T_1 values. While changing one parameter, other parameters were kept constant at $k = 25$, $n = 1$, and $TR_{gap} = 35$ ms. The vertical lines indicate our acquisition settings used at 3 T.

(Figure 3). It can be appreciated that the theoretical bias depends on the chosen settings and results in a substantial underestimation of T_1. The bias increases with fewer RF pulses per shot, early acquisition of the k-space center, and a longer temporal gap.

Furthermore, simulations show that signal to noise ratio and $B1^+$-inhomogeneities have similar effects in SPGR and I-SPGR T_1-mapping (Figures S1 and S2).

4.2 | VFA MRI

In the phantom and in vivo, the fit with the proposed signal model improved the accuracy of T_1-mapping, resulting in a reduction of the bias (Figures 4 and 5, respectively). In the phantom, the mean bias was −2% (centric) and 0% (linear) when fitted with the proposed model, which was substantially better than for the conventional approach when applied to I-SPGR VFA data (mean bias −35% (centric) and −21% (linear)). For reference, the mean bias in the phantom of the SPGR approach was −5%. The results at 1.5 T (Table S1 and Figure S4) follow the same pattern as at 3 T, where the fitting with the proposed model reduced the bias compared to fitting with the conventional model.

To validate Equation (8), for one experiment, we included acquisitions at high FAs, where both curves differ most (Figure 2). Indeed, the conventional model cannot be used to describe the observed signal increase as a function of FA for FAs > 30°. It can be seen that the fit with the conventional signal equation poorly follows the curve and introduces a substantial bias in the T_1 estimation. On the other hand, the proposed model describes the trend of the acquired signal at different flip angles more closely and provides accurate T_1 estimates. Interestingly, the shape of the I-SPGR curve (Equation (8)) resembles that of an SPGR curve (Equation (1)) at low FAs (2–25°), which are typically used in VFA experiments, but renders wrong T_1 values when fitted with the conventional signal model. This means that experiments performed with the typical FA (1–30°) will not spot discrepancies between the data and model, but measure inaccurate T1 values.

In the brain, the T_1 from I-SPGR VFA data fitted with the proposed signal equation was much closer to the reference T_1 than when using the conventional signal equation (T_1 bias with respect to conventional SPGR was −6% (−72 ms) versus −37% (−475 ms), respectively; Figure 5). This difference in T_1 was statistically significant ($P < 0.01$). The mean T1 ± standard deviation of the white matter was 1112 ± 193, 1017 ± 169, and 672 ± 125 ms with the SPGR, I-SPGR fitted with the proposed model, and I-SPGR fitted with the conventional model, respectively. For the gray matter, the mean T1 ± standard deviation was 1513 ± 395, 1468 ± 381, and 1006 ± 310 ms. Figure 5 also shows a representative T_1 map of one subject in an I-SPGR VFA sequence, compared to the T_1 map resulting from an SPGR VFA sequence, demonstrating high improvements in T_1 estimation bias for the proposed approach.

4.3 | DCE MRI

In simulations and in vivo, the use of the conventional signal model in an I-SPGR acquisition resulted in an increased value of the measured contrast concentration (Figure 6). In vivo, the mean difference in concentration over all time points was 48% for a randomly selected spleen voxel (Figure 6A). As can be seen, the in vivo data points of this pixel overlap with the simulated data points (Figure 6B).

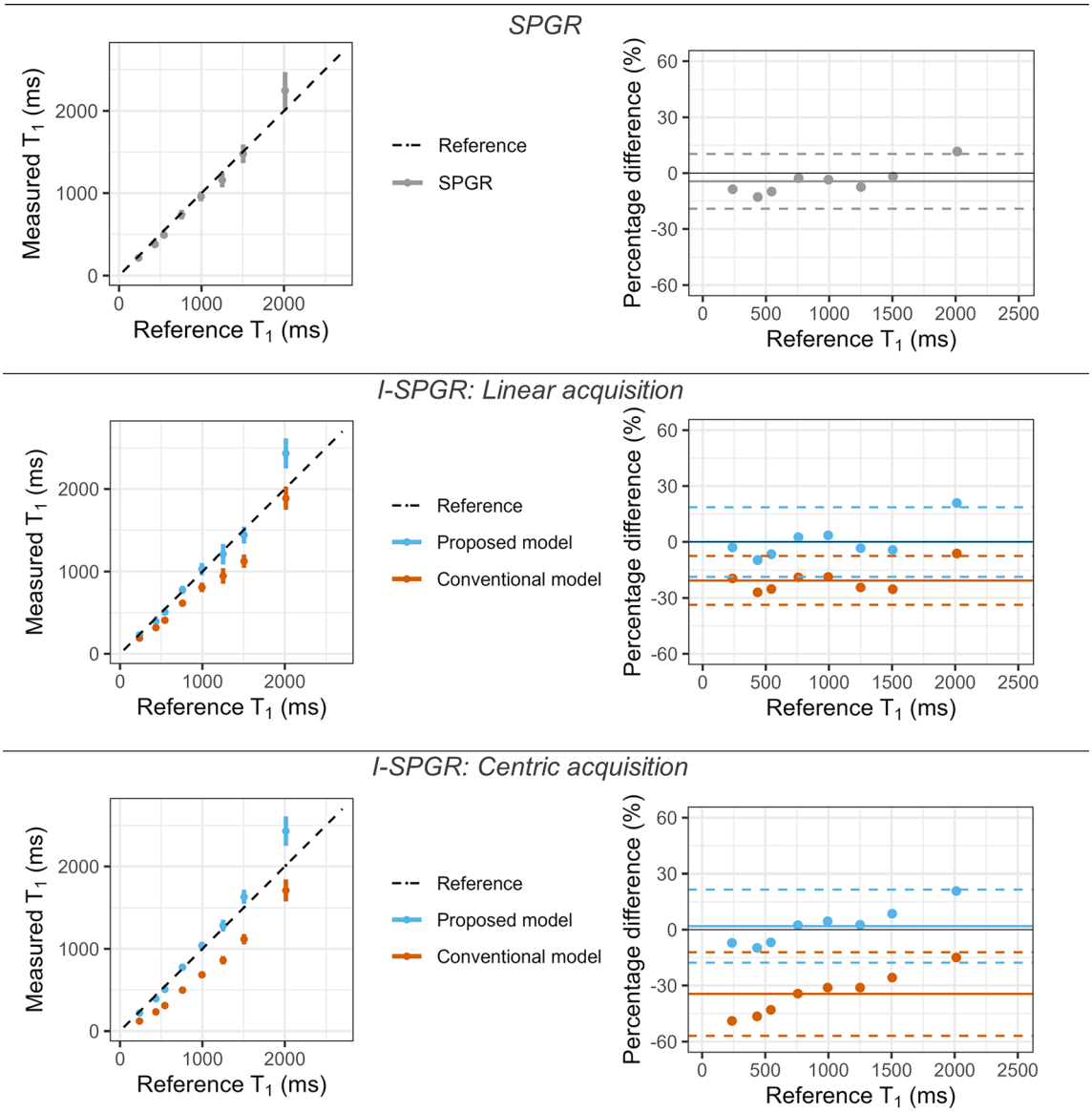

FIGURE 4 Results of T_1-mapping of the gold standard phantom at 3 T using SPGR (top row), linear ($n = 13$, middle row), and centric ($n = 1$, bottom row) I-SPGR acquisitions. In the left panels, the error bars indicate the 95% confidence interval within each region of interest. The reference T_1 values were taken from the phantom's manual. Bland–Altman plots are shown on the right.

It is feasible to use the proposed model for in vivo DCE (Figure 7). Overall, the use of the proposed model resulted in a small increase in every pharmacokinetic parameter compared to the conventional approach when using the individual AIF, but a large decrease in K^{trans}, v_e, and v_p and an increase in k_{ep} when using the population AIF. Particularly, for the spleen ROI shown, we saw an increase of 4%, 4%, 1%, and 0% for K^{trans}, k_{ep}, v_e, and v_p, respectively in the individual AIF case and a decrease of 35%, 32%, and 29% for K^{trans}, v_e, and v_p and an increase of 2% of k_{ep} with the population AIF.

5 | DISCUSSION

We have demonstrated that including the effect of the temporal gap from I-SPGR into the conventional SPGR signal equation is a simple solution for including preparation pulses in a VFA or DCE MRI acquisition. The proposed signal equation results in a more accurate T_1 estimate and DCE contrast concentration estimate from I-SPGR acquisitions than when using the conventional model. The method allows accurate T_1 estimations from I-SPGR acquisitions which, among other things, enables fat suppression and saturation bands, for improving the image quality of T_1-mapping and DCE MRI. Although such sequences are already widely available on MR scanners, guidelines currently advise against using them due to the

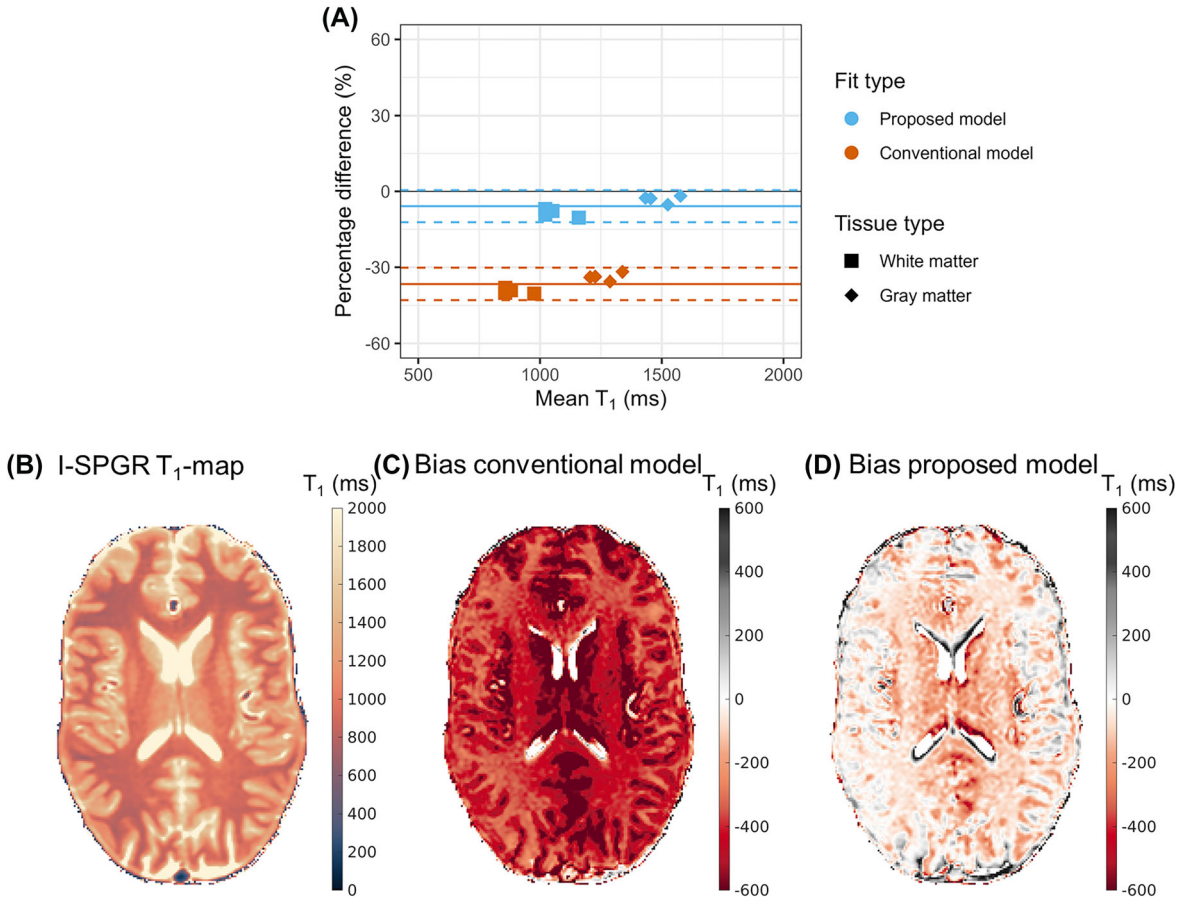

FIGURE 5 Bland–Altman plot of in vivo results in the brain of four healthy volunteers separated for white and gray matter. For every healthy volunteer, results from a region of interest in the white (square) and gray matter (triangle) are displayed (A). Results are shown for a fit using the conventional model (orange) and the proposed model (blue). An SPGR VFA sequence was used as a reference. (B) T_1 map of one subject for an I-SPGR sequence and the difference compared to an SPGR VFA sequence fitted with the conventional signal model (C) and proposed signal model (D).

lack of a correct signal equation.[15] With the proposed model, sequences such as fat-suppressed GRASP, VFA, and DCE MRI can be used for quantitative MRI without introducing a bias.

The proposed signal model results in accurate T_1 estimations in phantom measurements and in vivo, while the conventional signal model results in a large bias. The bias of using the conventional model in I-SPGR acquisitions is in the same order of magnitude as was predicted by simulations (Figure 3). The T_1 values measured in vivo in white and gray matter (Figure 5) were in the same order of magnitude as mentioned in the literature, although a large range of T_1 is reported.[29]

The estimated bias in the phantom of the VFA acquisition with the I-SPGR sequence and fitted to the proposed signal model (0% and −2%) and with SPGR acquisition and conventional model (−5%) is smaller compared to previous studies. As this is the first study where VFA T_1-mapping is performed in the Gold Standard phantom, the results can only be compared to results in other phantoms. Bane et al (2018) found a median bias of 32.2% and 8% at 3 T on a Philips Ingenia scanner and 1.5 T on a Siemens Aera scanner, respectively.[30] Keenan et al (2021) report a bias of up to 35% at 3 T and up to 20% at 1.5 T, depending on the vendor.[31] Tirkes et al (2019) found a mean bias of 9.2%[32] and Wang et al (2021) measured 6.3–14.6%, depending on the scanner.[33]

Several sequence settings can reduce the effect of the interruption of the steady-state on the signal, including reducing the duration of TR_{gap}, measuring the central k-line later in the RF train, and increasing the shot length (Figure 3). Particularly, we verified that measuring the central k-line later in the RF pulse train (i.e. $n > 1$) resulted in lower mean bias (−21%) for the I-SPGR linear k-space ($n = 13$) filling at 3 T when compared to the centric k-space filling (−35%) ($n = 1$) (Figure 4). Note, however, that increasing shot length and increasing n reduce the effect of the preparation pulses on the image. Moreover, reducing TR_{gap} is not always possible due to SAR constraints and preparation pulse length.

The proposed signal model also removes biases of up to 48% in the contrast concentrations measured with I-SPGR-acquired DCE MRI (Figure 6). In literature, a range of pharmacokinetic parameters in the spleen is mentioned: K^{trans} 0.64–1.19 min^{-1}, k_{ep} 1.40–1.86 min^{-1}, v_e 0.42–0.46, v_p 0.03–0.05.[34,35] The values found in this work are in the same order of magnitude (Figure 7). Additionally, the summation of v_e and v_p

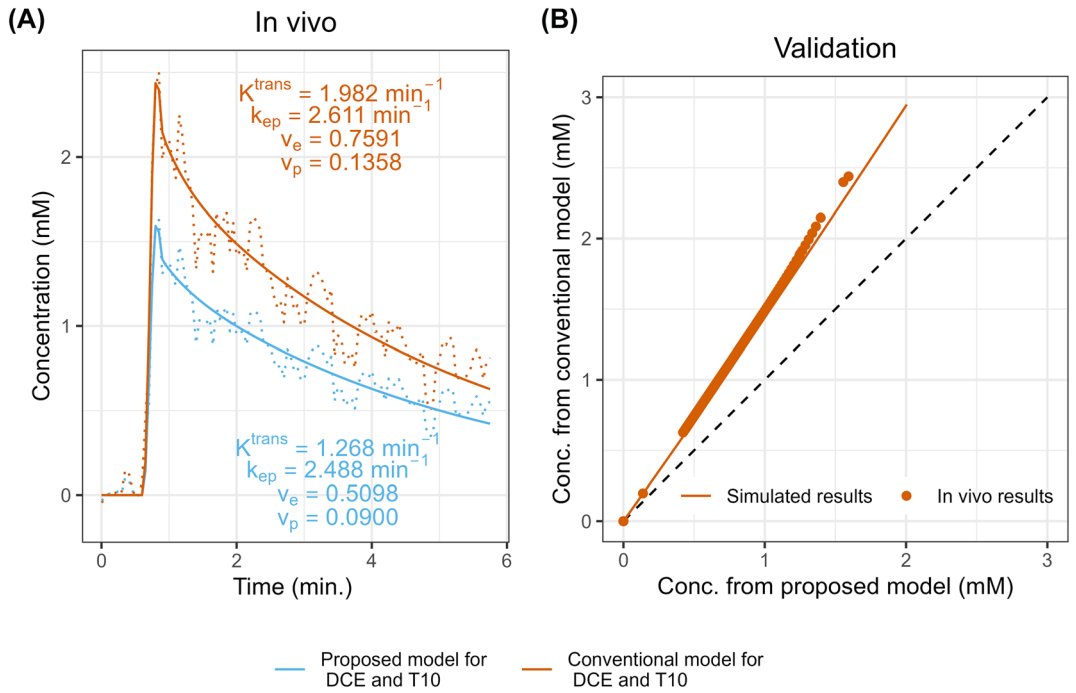

FIGURE 6 Difference in concentration estimated with the conventional model (orange line) and proposed model (blue lines) in vivo (A) and in simulation (B). In vivo, the concentration curves were taken from a voxel in the spleen. The original data is plotted as a dotted line, while the resulting fit (using a population-based AIF) is shown as a solid line. In panel B, the in vivo results from panel A are plotted together with the results from the simulation. In the simulation, the signal was modeled using the proposed model with the acquisition settings as used in panel A, and the concentration was computed with the conventional model.

results in the extracellular volume. In literature, the extracellular volume was found to be 0.26 and 0.34 using inversion-based T_1-mapping and equilibrium DCE, respectively.[36,37] The results in this work are in line with these values, except for the conventional model combined with the population-based AIF.

Although the measured contrast concentration and pharmacokinetic parameters cannot be compared to ground truth or reference values, simulations show that the use of the conventional signal model in the I-SPGR case introduces this bias, if we assume that the proposed signal model is correct. Indeed, the results in vivo overlap with the simulated results (Figure 6B). In fact, the correction is needed twice, once when determining T_{10} with VFA T_1-mapping, and once during the actual DCE acquisition. If ignored, the measured contrast concentrations are overestimated substantially (Figures 6 and 7), resulting in a change in pharmacokinetic parameter estimates. It should be noted that the difference in pharmacokinetic parameters estimates is small when using an individual AIF, because the overestimation of contrast concentration that occurs in the AIF compensates for the overestimation in contrast concentration in the tissue when using the conventional model and in this case "two wrongs" do "make a right". This effect of the individual AIF can also be appreciated in Figure 6A, where the pharmacokinetic parameters are similar for both models, but the concentration curves are different.

5.1 | Practical use of the proposed signal model

We measured the accuracy of the signal model at different field strengths (results at 1.5 T can be found in the Supplemental Material, Figure S2), in two vendors using phantom and in vivo measurements. However, the model requires knowledge of the acquisition order in k-space (defining n) and the shot length (defining k); parameters that are not typically considered and not always saved in the DICOM header. Hence, we advise users to log these parameters when scanning. The number of start-up echoes (also called dummy echoes) must be added to the TFE/Turbo factor to compute the final parameter k in Equation (8) using

$$n_{centric} = 1 + start\ up\ echoes. \tag{13}$$

One must consider that the use of partial Fourier acquisition changes the parameter n for linear k-space filling. For linear k-space-filling, the n is determined by the partial Fourier factor as the lines per shot (LPS) minus half of the lines skipped by partial Fourier:

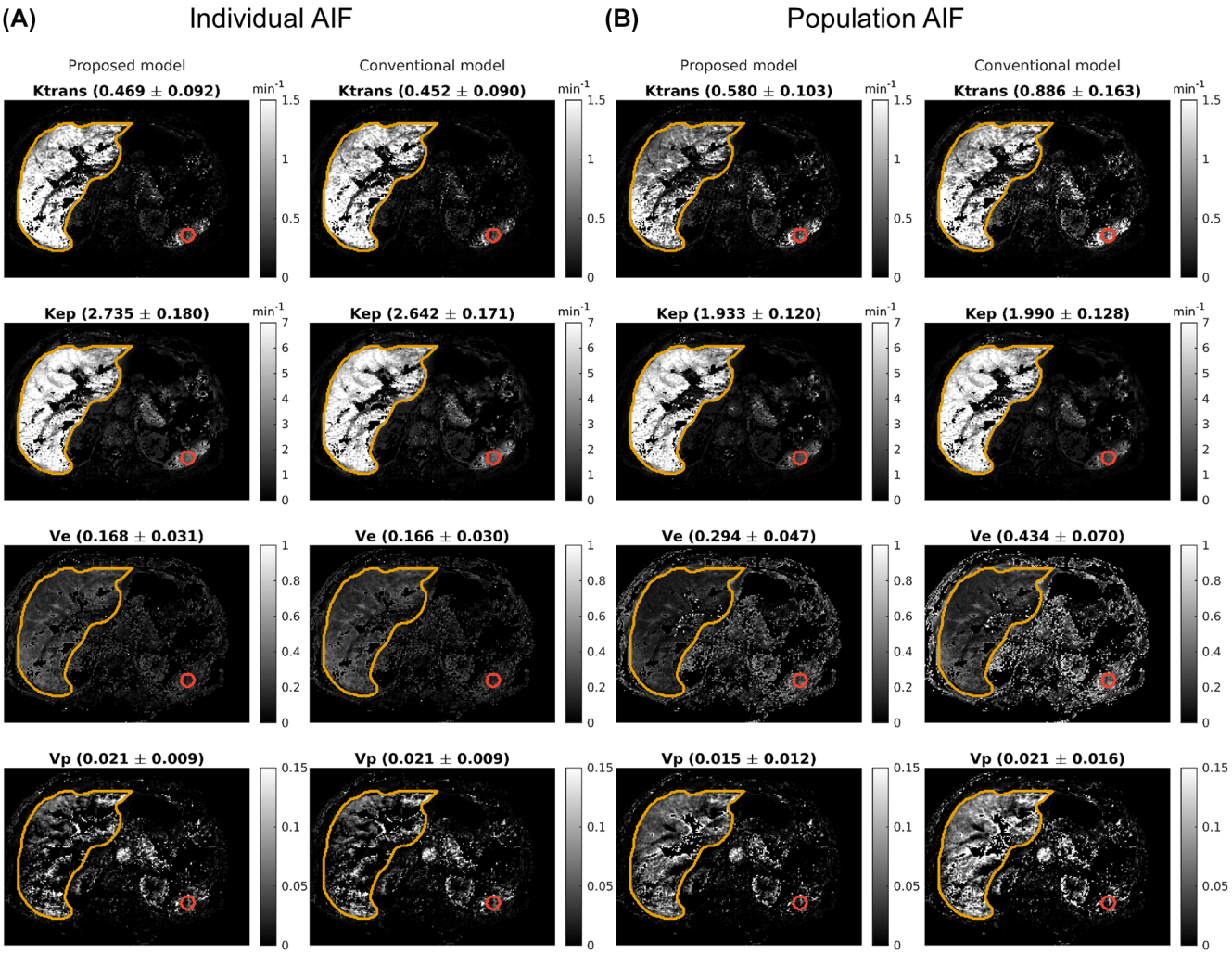

FIGURE 7 Parameters of DCE MRI in the abdomen of a healthy volunteer, with A the results when an individualized AIF is used and B with a population-based AIF. In both cases, the left column represents the parameter maps when using the proposed model and the right column displays the results with the conventional model. The mean and standard deviation within a region of interest in the spleen (circled in red) are presented in the title of the images. Furthermore, the mask of the liver where the dual inlet model was used is drawn in yellow.

$$n_{linear} = round\left(LPS - \frac{\frac{LPS}{partial\ Fourier\ factor}}{2} + start\ up\ echoes\right). \tag{14}$$

LPS is defined as lines acquired in k-space, not including start-up echoes.

It is furthermore important to note that we could not invert the proposed signal model. Therefore, we could not derive an equation that directly relates the T_1 value to the acquired signal, analog to conventional SPGR. This implies the need for fitting T_1 at every time step in a DCE acquisition, based on the baseline M_0 map, using a linear, single-parameter fit. This process is more time-consuming but can be accelerated by using the T_1 fitted in the previous timestep as initial guess. Additionally, we excluded voxels without a reliable T_1, defined as being within a range of 100 to 2000 ms, from the analysis.

5.2 | Limitations

There were some limitations to this work. First, no correction for inhomogeneities in the $B1^+$-field was performed. Previous research has shown that this significantly improves the accuracy of VFA T_1-mapping, especially at 3 T.[38–42] Optimization of $B1^+$_field mapping proved a challenge on two scanners, which was also noted in other research.[30,31,43–45] This was the main reason for not performing the correction. Additionally, the

effect of $B1^+$-inhomogeneities is expected to be smaller in I-SPGR-type sequences compared to SPGR (Figure S2), so we do not expect a bias in our comparison of both models.

Secondly, it must be noted that our approach is only valid in sequences where the preparation pulses in the temporal gap do not affect the magnetization of the spins of interest. Thus, preparations such as inversion pulses, which would result in a more MP2RAGE-type of sequence,[20,21] are not included. In the future, other acquisition schemes may also be tested to estimate T_1, for example by varying parameters *k*, *n*, or the temporal gap length instead of the FA.

Thirdly, the signal model assumes that image contrast is only determined by data acquired in the center of the k-space. In practice, however, image contrast is also determined by data acquired around the k-space center. This implies that the effect of the temporal gap can be over- and underestimated, depending on which value for *n* is chosen. In the future, strategies for compensating for this effect can be investigated, for example by assuming an empirically determined "effective" *n* at which contrast is defined, instead.

Fourthly, we used the T_1 measured with a conventional VFA sequence as reference values in vivo, while inversion-recovery-based T_1 can also be used. We made this choice because other T_1-mapping methods can introduce new biases that do not arise from the use of an incorrect signal model, but are inherent to the method. The proposed signal model should describe the I-SPGR sequence in a similar fashion as the conventional signal model applies to an SPGR sequence, and hence we chose the conventional SPGR acquisition as a reference.

Lastly, we ignored the effect of spoiling in this work. In general, VFA T_1-mapping is susceptible to errors introduced by insufficient spoiling of the transverse magnetization.[46] However, given the good agreement between the theory and experiments, we do not expect that spoiling had a substantial effect. Moreover, I-SPGR sequences are expected to be less affected by imperfect spoiling than SPGR sequences, due to the additional gap in the steady-state during which imperfectly spoiled spins undergo T_2-relaxation.

6 | CONCLUSION

We have derived the signal equation for interrupted spoiled gradient echo and illustrated its need. With this equation, essential preparation pulses such as fat suppression and saturation bands can be added to VFA T_1-mapping and DCE without the loss of accuracy. This will allow for performing VFA T_1-mapping and DCE using popular sequences such as GRASP.

ACKNOWLEDGMENTS

This work was supported by ZonMW grant 09120011910004 and KWF-UVA grant 2021.13785.

DATA AVAILABILITY STATEMENT

The data acquired for this work are available upon reasonable request to the corresponding author.

ORCID

Myrte Wennen https://orcid.org/0000-0002-7749-936X
Joost P. A. Kuijer https://orcid.org/0000-0002-4181-0427
Gustav J. Strijkers https://orcid.org/0000-0001-6700-5058

REFERENCES

1. Gurney-Champion OJ, Mahmood F, van Schie M, et al. Quantitative imaging for radiotherapy purposes. *Radiother Oncol*. 2020;146:66-75. doi:10.1016/j.radonc.2020.01.026
2. Klaassen R, Steins A, Gurney-Champion OJ, et al. Pathological validation and prognostic potential of quantitative MRI in the characterization of pancreas cancer: preliminary experience. *Mol Oncol*. 2020;14(9):2176-2189. doi:10.1002/1878-0261.12688
3. Gordon Y, Partovi S, Müller-Eschner M, et al. Dynamic contrast-enhanced magnetic resonance imaging: fundamentals and application to the evaluation of the peripheral perfusion. *Cardiovasc Diagn Ther*. 2014;4(2):147-164. doi:10.3978/j.issn.2223-3652.2014.03.01
4. Sujlana P, Skrok J, Fayad LM. Review of dynamic contrast-enhanced MRI: technical aspects and applications in the musculoskeletal system. *J Magn Reson Imaging*. 2018;47(4):875-890. doi:10.1002/jmri.25810
5. Burt JR, Zimmerman SL, Kamel IR, Halushka M, Bluemke DA. Myocardial T1 mapping: techniques and potential applications. *Radiographics*. 2014;34(2):377-395. doi:10.1148/rg.342125121
6. Anzalone N, Castellano A, Cadioli M, et al. Brain gliomas: multicenter standardized assessment of dynamic contrast-enhanced and dynamic susceptibility contrast MR images. *Radiology*. 2018;287(3):933-943. doi:10.1148/radiol.2017170362
7. Verma S, Turkbey B, Muradyan N, et al. Overview of dynamic contrast-enhanced MRI in prostate cancer diagnosis and management. *AJR am J Roentgenol*. 2012;198(6):1277-1288. doi:10.2214/AJR.12.8510
8. Kataoka M, Honda M, Sagawa H, et al. Ultrafast dynamic contrast-enhanced MRI of the breast: from theory to practice. *J Magn Reson Imaging*. 2024;60(2):401-416. doi:10.1002/jmri.29082
9. Kousi E, Smith J, Ledger AE, et al. Quantitative evaluation of contrast agent uptake in standard fat-suppressed dynamic contrast-enhanced MRI examinations of the breast. *Med Phys*. 2018;45(1):287-296. doi:10.1002/mp.12652

10. Vivoda Tomšič M, Bisdas S, Kovač V, Serša I, Šurlan PK. Dynamic contrast-enhanced MRI of malignant pleural mesothelioma: a comparative study of pharmacokinetic models and correlation with mRECIST criteria. *Cancer Imaging*. 2019;19(1):10. doi:10.1186/s40644-019-0189-5
11. Miyazaki M, Wheaton A, Kitane S. Enhanced fat suppression technique for breast imaging. *J Magn Reson Imaging*. 2013;38(4):981-986. doi:10.1002/jmri.23932
12. Feng L. Golden-angle radial MRI: basics, advances, and applications. *J Magn Reson Imaging*. 2022;56(1):45-62. doi:10.1002/jmri.28187
13. Le Y, Dale B, Akisik F, Koons K, Lin C. Improved T1, contrast concentration, and pharmacokinetic parameter quantification in the presence of fat with two-point Dixon for dynamic contrast-enhanced magnetic resonance imaging. *Magn Reson Med*. 2016;75(4):1677-1684. doi:10.1002/mrm.25639
14. Ikeno H, Sakai K, Imai H, et al. Effects of different fat-suppression methods on T1 values in dynamic contrast-enhanced magnetic resonance imaging: a phantom study. *Radiol Phys Technol*. 2019;12(3):335-342. doi:10.1007/s12194-019-00521-x
15. Committee DMT. *DCE MRI Quantification Profile (1.0)*. Quantitative Imaging Biomarkers Alliance; 2012.
16. Deng H-P, Li X-M, Yang L, et al. DCE-MRI of esophageal carcinoma using star-VIBE compared with conventional 3D-VIBE. *Sci Rep*. 2021;11(1):24091. doi:10.1038/s41598-021-03171-5
17. Higashi M, Tanabe M, Okada M, Furukawa M, Iida E, Ito K. Influence of fat deposition on T1 mapping of the pancreas: evaluation by dual-flip-angle MR imaging with and without fat suppression. *Radiol Med*. 2020;125(1):1-6. doi:10.1007/s11547-019-01087-9
18. White JC, Sinha S, Sinha U. Spin lattice (T1) and magnetization transfer saturation (MTsat) imaging to monitor age-related differences in skeletal muscle tissue. *Diagnostics*. 2022;12(3):584. doi:10.3390/diagnostics12030584
19. Brix G, Schad LR, Deimling M, Lorenz WJ. Fast and precise T1 imaging using a TOMROP sequence. *Magn Reson Imaging*. 1990;8(4):351-356. doi:10.1016/0730-725X(90)90041-Y
20. Nie Y, Lu N, Liao L, et al. Black-blood magnetization prepared 2 rapid acquisition gradient echoes: a fast and three-dimensional MR black-blood T1 mapping technique for quantitative assessment of atherosclerosis and venous thrombosis. *J Magn Reson Imaging*. 2023;60(3):1148-1162. doi:10.1002/jmri.29156
21. Marques JP, Kober T, Krueger G, van der Zwaag W, Van de Moortele P-F, Gruetter R. MP2RAGE, a self bias-field corrected sequence for improved segmentation and T1-mapping at high field. *Neuroimage*. 2010;49(2):1271-1281. doi:10.1016/j.neuroimage.2009.10.002
22. Tofts PS. Modeling tracer kinetics in dynamic Gd-DTPA MR imaging. *J Magn Reson Imaging*. 1997;7(1):91-101. doi:10.1002/jmri.1880070113
23. Szomolanyi P, Rohrer M, Frenzel T, et al. Comparison of the relaxivities of macrocyclic gadolinium-based contrast agents in human plasma at 1.5, 3, and 7 T, and blood at 3 T. *Invest Radiol*. 2019;54(9):559-564. doi:10.1097/RLI.0000000000000577
24. Marquardt DW. An algorithm for least-squares estimation of nonlinear parameters. *J Soc Ind Appl Math*. 1963;11(2):431-441. doi:10.1137/0111030
25. Feng L, Huang C, Shanbhogue K, Sodickson DK, Chandarana H, Otazo R. RACER-GRASP: respiratory-weighted, aortic contrast enhancement-guided and coil-unstreaking golden-angle radial sparse MRI. *Magn Reson Med*. 2018;80(1):77-89. doi:10.1002/mrm.27002
26. Dickie BR, Ahmed Z, Arvidsson J, et al. A community-endorsed open-source lexicon for contrast agent-based perfusion MRI: a consensus guidelines report from the ISMRM Open Science initiative for perfusion imaging (OSIPI). *Magn Reson Med*. 2024;91(5):1761-1773. doi:10.1002/mrm.29840
27. Orton MR, d'Arcy JA, Walker-Samuel S, et al. Computationally efficient vascular input function models for quantitative kinetic modelling using DCE-MRI. *Phys Med Biol*. 2008;53(5):1225-1239. doi:10.1088/0031-9155/53/5/005
28. Yang JF, Zhao ZH, Zhang Y, et al. Dual-input two-compartment pharmacokinetic model of dynamic contrast-enhanced magnetic resonance imaging in hepatocellular carcinoma. *World J Gastroenterol*. 2016;22(13):3652-3662. doi:10.3748/wjg.v22.i13.3652
29. Bojorquez JZ, Bricq S, Acquitter C, Brunotte F, Walker PM, Lalande A. What are normal relaxation times of tissues at 3 T? *Magn Reson Imaging*. 2017;35:69-80. doi:10.1016/j.mri.2016.08.021
30. Bane O, Hectors SJ, Wagner M, et al. Accuracy, repeatability, and interplatform reproducibility of T1 quantification methods used for DCE-MRI: results from a multicenter phantom study. *Magn Reson Med*. 2018;79(5):2564-2575. doi:10.1002/mrm.26903
31. Keenan KE, Gimbutas Z, Dienstfrey A, et al. Multi-site, multi-platform comparison of MRI T1 measurement using the system phantom. *PLoS ONE*. 2021;16(6):e0252966. doi:10.1371/journal.pone.0252966
32. Tirkes T, Zhao X, Lin C, et al. Evaluation of variable flip angle, MOLLI, SASHA, and IR-SNAPSHOT pulse sequences for T(1) relaxometry and extracellular volume imaging of the pancreas and liver. *Magma*. 2019;32(5):559-566. doi:10.1007/s10334-019-00762-2
33. Wang Y, Tadimalla S, Rai R, et al. Quantitative MRI: defining repeatability, reproducibility and accuracy for prostate cancer imaging biomarker development. *Magn Reson Imaging*. 2021;77:169-179. doi:10.1016/j.mri.2020.12.018
34. Wassenaar NPM, Gurney-Champion OJ, van Schelt A-S, et al. Optimizing pseudo-spiral sampling for abdominal DCE MRI using a digital anthropomorphic phantom. *Magn Reson Med*. 2024;92(5):2051-2064. doi:10.1002/mrm.30213
35. Holland MD, Morales A, Simmons S, et al. Disposable point-of-care portable perfusion phantom for quantitative DCE-MRI. *Med Phys*. 2022;49(1):271-281. doi:10.1002/mp.15372
36. Bandula S, Banypersad SM, Sado D, et al. Measurement of tissue interstitial volume in healthy patients and those with amyloidosis with equilibrium contrast-enhanced MR imaging. *Radiology*. 2013;268(3):858-864. doi:10.1148/radiol.13121889
37. Mesropyan N, Isaak A, Faron A, et al. Magnetic resonance parametric mapping of the spleen for non-invasive assessment of portal hypertension. *Eur Radiol*. 2021;31(1):85-93. doi:10.1007/s00330-020-07080-5
38. Lee Y, Callaghan MF, Nagy Z. Analysis of the precision of variable Flip angle T1 mapping with emphasis on the noise Propagated from RF transmit field maps. Original research. *Front Neurosci*. 2017;11:11. doi:10.3389/fnins.2017.00106
39. Sivertsson C, Chan J, Tiderius CJ, et al. Effects of B1 inhomogeneity correction for three-dimensional variable flip angle T1 measurements in hip dGEMRIC at 3 T and 1.5 T. *Magn Reson Med*. 2012;67(6):1776-1781. doi:10.1002/mrm.23150
40. Liberman G, Louzoun Y, Ben BD. T_1 mapping using variable flip angle SPGR data with flip angle correction. *J Magn Reson Imaging*. 2014;40(1):171-180. doi:10.1002/jmri.24373
41. Sengupta A, Gupta RK, Singh A. Evaluation of B1 inhomogeneity effect on DCE-MRI data analysis of brain tumor patients at 3T. *J Transl Med*. 2017;15(1):242. doi:10.1186/s12967-017-1349-7
42. Cho YJ, Kim WS, Choi YH, et al. Validation and feasibility of liver T1 mapping using free breathing MOLLI sequence in children and young adults. *Sci Rep*. 2020;10(1):18390. doi:10.1038/s41598-020-74717-2
43. Boudreau M, Tardif CL, Stikov N, Sled JG, Lee W, Pike GB. B(1) mapping for bias-correction in quantitative T(1) imaging of the brain at 3T using standard pulse sequences. *J Magn Reson Imaging*. 2017;46(6):1673-1682. doi:10.1002/jmri.25692

44. Tadimalla S, Wilson DJ, Shelley D, et al. Bias, repeatability and reproducibility of liver T1 mapping with variable Flip angles. *J Magn Reson Imaging*. 2022;56(4):1042-1052. doi:10.1002/jmri.28127
45. Bliesener Y, Zhong X, Guo Y, et al. Radiofrequency transmit calibration: a multi-center evaluation of vendor-provided radiofrequency transmit mapping methods. *Med Phys*. 2019;46(6):2629-2637. doi:10.1002/mp.13518
46. Preibisch C, Deichmann R. Influence of RF spoiling on the stability and accuracy of T1 mapping based on spoiled FLASH with varying flip angles. *Magn Reson Med*. 2009;61(1):125-135. doi:10.1002/mrm.21776

SUPPORTING INFORMATION

Additional supporting information can be found online in the Supporting Information section at the end of this article.

How to cite this article: Wennen M, Stehling W, Marcus JT, et al. A signal model for fat-suppressed T_1-mapping and dynamic contrast-enhanced MRI with interrupted spoiled gradient-echo readout. *NMR in Biomedicine*. 2025;38(1):e5289. doi:10.1002/nbm.5289